Hexagonal phase ordering in strongly segregated copolymer films

Karl Glasner
Department of Mathematics, University of Arizona, Tucson, Arizona 85721, USA
(Received 15 June 2015; published 8 October 2015)

Strongly segregated copolymer mixtures with uneven composition ratio can form hexagonally ordered thin films. A simplified model describing the size and position of micellelike clusters is derived, allowing for investigation of much larger domain sizes than in previous studies. Simulations of this model are performed to study the generation of large scale order and evolution of pattern defects. We find three temporal regimes exhibiting different scaling laws for orientational correlation length and defect number. In the early stage, topological defects are rapidly eliminated by pairwise annihilation. A slower intermediate stage is characterized by the migration of grain boundaries and the elimination of small grains. In the final stage, grain boundaries become pinned and the evolution halts. A scaling law for defect interaction is proposed which is consistent with the crossover between the first and second stages.

DOI: 10.1103/PhysRevE.92.042602 PACS number(s): 36.20.−r, 61.72.Mm, 81.10.−h

Recent advances in nanoscale fabrication [1–4] have lead to growing interest in the theoretical aspects of molecular self-assembly [5,6]. Some of the most natural candidates for synthetic self-assembly are block copolymers because of the wide variety of possible stable morphologies [7–10]. Equilibrium patterns have been successfully predicted in the context of both self-consistent field theory [11] as well as density functional models [12]. In contrast, there are still many open questions about dynamics leading to large-scale order.

Block copolymer thin films have attracted considerable attention because they have desirable self-assembly properties [13]. Experiments on block copolymer thin films have been able to capture the time evolution of pattern defects and orientation domain coarsening [14–16]. They find in the case of a spherical or cylindrical phase that gives rise to hexagonally ordered films that the correlation length ξ characterizing the size of grains of similar orientation grows roughly according to the power law $t^{1/4}$, at least after some initial transient behavior. Simulations of this process by Yokojima and Shiwa [17] and Vega *et al.* [18] rely on cell dynamics models based on an Ohta-Kawasaki-type free energy functional. Both studies observe the formation of domains separated by grain boundaries composed of dislocations, which coarsen over time by virtue of annihilation of small domains. Over a limited time frame (about two decades), these studies tracked various measures of correlation lengths, and they find slightly different scaling exponents ranging from $1/5$ to $1/4$.

Since the largest correlation length in these previous studies was comparable to the domain width, system size might have played a role in the later stages of ordering. In addition, most theoretical studies of hexagonal ordering are limited to weakly segregated (in the case of polymers) or weakly nonlinear (for other pattern forming systems) regimes. This is not surprising since continuum models often become numerically intractable when nonlinear contributions are large and diffuse interfaces become narrow. These limitations suggest that a much different modeling paradigm is needed to properly investigate large systems which involve strongly segregated polymers. The route taken here is to employ a combination of sharp interface models and Lifshitz-Slyozov-Wagner (LSW) reduction, as done in [19,20]. We derive a model suitable for two dimensional films which allows for much larger system sizes than those in past investigations.

The dynamics of hexagonal ordering has also been investigated in other physical systems. Recent studies [21,22] of the phase field crystal equation [23] have shown the development and coarsening of orientation domains analogous to copolymer films. In this case, a wide variety of scaling exponents may be observed [21] which is dependent on a parameter describing the depth of the quench which leads to crystallization. Dynamic scaling of pattern domains has also been studied in the context of convection patterns [24–27]. Scaling exponents in these studies range from $1/5$ to $1/3$, depending on how far the system was from onset of instability and whether noise was included. Mechanisms which might contribute to slow coarsening such as pinning of dislocations [28] have been proposed. There is, however, no definitive explanation of slow coarsening in these systems.

This paper systematically derives a dynamical model for the size and position of roughly circular domains in a strongly segregated asymmetric block copolymer mixture. We observe that this highly coupled system has a screening property which allows the spatial domain to be decomposed into subdomains, yielding a tractable method for large scale simulation. The system incorporates both Ostwald ripening behavior of domains and domain repulsion which leads to ordering dynamics. Simulations are conducted over large space and time scales to observe several stages of ordering processes each characterized by a different dynamic scaling exponent. A scaling model of dislocation dynamics is presented which unifies these separate regimes. Finally, relationships to experimental work are discussed.

I. DENSITY FUNCTIONAL MODELS AND THEIR SHARP INTERFACE LIMIT

Density functional models [29–31] have been implemented extensively to study large scale pattern formation in block copolymers. They have generally been preferred over self-consistent field theory approaches (see, e.g., [9]) for large simulations because they offer much greater numerical efficiency. On the other hand, in the strong segregation limit either model becomes intractable because of the need to resolve small

interfacial scales. As a point of departure, we will instead use the free boundary evolution that arises as the sharp interface limit.

For $A-B$ diblock mixtures occupying a domain Ω, a typical free energy functional for the relative A monomer fraction $\phi:\Omega\to[0,1]$ has the form [29]

$$F(\phi)=\int_\Omega \frac{\epsilon^2}{2}|\nabla\phi|^2+W(\phi)\,d\mathbf{x}+\frac{\sigma}{2}\int_\Omega\int_\Omega G(\mathbf{x}-\mathbf{x}')\times[\phi(\mathbf{x})-f][\phi(\mathbf{x}')-f]\,d\mathbf{x}\,d\mathbf{x}'. \tag{1}$$

The first integral describes local interactions among monomers which promote phase separation. The term $W(\phi)$ is a typical double-well potential preferring $\phi=0$ and $\phi=1$. The last term describes nonlocal interactions, where f is the global volume fraction and the interaction kernel G is typically a Laplacian Green's function. Dynamics associated with Eq. (1) arise from gradients of the chemical potential $\delta F/\delta\phi$. This leads to a modification of the well-known Cahn-Hilliard equation of the form

$$M^{-1}\phi_t=\Delta[-\epsilon^2\,\Delta\phi+W'(\phi)]-\sigma(\phi-f), \tag{2}$$

where M is a kinetics dependent mobility.

As mentioned in the introduction, the continuum model (2) becomes intractable for small ϵ or equivalently large segregation associated with a high potential barrier in the bulk free energy $W()$. As is typical of phase field approaches, the sharp interface limit of Eq. (2) may be sought as a distinguished limit of parameters, in this case by scaling $M^{-1}\propto\epsilon$ and $\sigma=\gamma\epsilon$. The singular limit $\epsilon\to0$, first computed by Nishiura and Ohnishi [32], results in a free boundary problem for phase domains Ω^+,Ω^-, where Ω^+ denotes the minority phase. The free boundary, denoted $\partial\Omega^+$, evolves according to the nonlocal problem

$$\Delta v=\gamma\begin{cases}1-f & \text{in }\Omega^+\\ -f & \text{in }\Omega^-,\end{cases} \tag{3}$$

$$v=\kappa \text{ on } \partial\Omega^+, \tag{4}$$

$$V_n=[\partial v/\partial n]^-_+, \tag{5}$$

where the convention is used that the normal velocity V_n and mean curvature κ are outward with respect to Ω^+. Similar free boundary evolutions have been considered elsewhere in the context of other nonlocal interaction terms [19,33]. We use Eqs. (3)–(5) as a point of departure for a further reduction of the dynamics.

II. A FINITE DIMENSIONAL REDUCTION OF THE FREE BOUNDARY EVOLUTION

For small to moderate volume fractions, two dimensional hexagonal domain patterns are formed from roughly circular patches, and a LSW-type approximation [34,35] of the free boundary problem can be carried out. This has been done previously for other long range interactions [19] and for the spherical phase of three dimensional block copolymers [20]. We pursue here the same strategy for the two dimensional free boundary problem.

For the remainder of this paper, the spatial domain is taken to be a square $\Omega=[-L/2,L/2]^2$ with periodic boundary conditions, mimicking a large system absent of confinement effects. Note that a square domain is incommensurate with exact hexagonal packing, although this mismatch is very small provided the domain is large enough. In addition, we find that hexagonal ordering is only established on subdomains (grains) which are always much smaller than the system size.

The minority phase domain will be taken to be a collection of nonoverlapping disks (hereafter called particles):

$$\Omega^+=\cup_{i=1}^N B(\mathbf{x}_i;R_i), \tag{6}$$

where $\mathbf{x}_i$ are the particle centers and R_i are their radii. The approximation which follows relies on the typical radius R being small compared to the typical interparticle distance d.

A. Particle dynamics for small volume fraction

Let $G(\mathbf{x})$ be the modified Green's function satisfying

$$-\Delta G=\delta(\mathbf{x})-\frac{1}{|\Omega|}, \tag{7}$$

subject to periodic boundary conditions $G(\mathbf{x})=G(\mathbf{x}+L\mathbf{m})$ where $\mathbf{m}\in\mathbb{Z}^2$ ($|\Omega|$ denotes the area of the domain Ω). Note that one can decompose the Green's function into free space and smooth regular parts:

$$G(\mathbf{x})=-\frac{1}{2\pi}\ln(|\mathbf{x}|)+G_R(\mathbf{x}),\quad G_R(\mathbf{x})=O(1)\text{ as }|\mathbf{x}|\to0. \tag{8}$$

The leading order approximation for $R\ll d$ of the solution of Eq. (3) in the majority phase subdomain Ω_- is

$$v(\mathbf{x})=A_0+\sum_{i=1}^N A_i G(\mathbf{x}-\mathbf{x}_i),\quad \mathbf{x}\in\Omega^-, \tag{9}$$

where

$$\sum_{i=1}^N A_i=-\gamma f|\Omega|=-\gamma|\Omega^+|. \tag{10}$$

Implementing the boundary condition (4) gives

$$\frac{1}{R_i}=A_0-\frac{A_i}{2\pi}\ln R_i+\sum_{j=1,j\neq i}^N A_j G(\mathbf{x}_i-\mathbf{x}_j), \tag{11}$$

where Eq. (8) and the approximation $G(\mathbf{x}_i-\mathbf{x}_j)\approx G(\mathbf{x}-\mathbf{x}_j)$ for $\mathbf{x}\in\partial B_i$ were used. Equations (10) and (11) form a $(N+1)\times(N+1)$ linear system for the coefficients A_i.

Inside each particle $B(\mathbf{x}_i;R_i)$, the solution to Eqs. (3) and (4) is $v=\gamma|\mathbf{x}-\mathbf{x}_i|^2/4-\gamma R_i^2/4+R_i^{-1}$. The normal derivatives to the free boundary can therefore be approximated (again using $R\ll d$) as

$$\partial v/\partial n|_+=\frac{\gamma R_i}{2},\quad \left.\frac{\partial v}{\partial n}\right|_-=-\frac{A_i}{2\pi R_i}, \tag{12}$$

where $|_\pm$ refers to one-sided limits from the subdomains $\Omega_\pm$.

To determine the motion of particles, the boundary layer of the field v near each particle must be found by further expanding

$$v\sim A_i G(\mathbf{x}-\mathbf{x}_i)+v_1,\quad \Delta v_1=0,$$
$$v_1=0\quad\text{when}\quad|\mathbf{x}-\mathbf{x}_i|=R_i. \tag{13}$$

Formally matching the expansion to the field far away from the boundary layer given by Eq. (9) requires that

$$\nabla v_1 \cdot (\mathbf{x} - \mathbf{x}_i) \sim \psi \cdot (\mathbf{x} - \mathbf{x}_i), \quad |\mathbf{x}| \to \infty, \tag{14}$$

where

$$\psi = \sum_{j=1, j\neq i}^{N} A_j \nabla G(\mathbf{x}_i - \mathbf{x}_j). \tag{15}$$

The solution for the correction term v_1 in Eq. (13) satisfying Eq. (14) is

$$v_1 = \psi \cdot (\mathbf{x} - \mathbf{x}_i)\left(1 - R_i^{-2}|\mathbf{x} - \mathbf{x}_i|^2\right), \tag{16}$$

whereas the correction term inside each particle is $v_1 = 0$. Using Eq. (12), the expression for the interface velocity Eq. (5) is therefore

$$V_n = \left[\frac{\partial v}{\partial n}\right]_+^- = -\left[\frac{A_i}{2\pi R_i} + \frac{\gamma R_i}{2}\right] + \frac{2}{R_i}\psi \cdot (\mathbf{x} - \mathbf{x}_i), \quad \mathbf{x} \in \partial B_i. \tag{17}$$

The first term in this expression is isotropic and provides radial dynamics:

$$\dot{R}_i = -\frac{A_i}{2\pi R_i} - \frac{\gamma R_i}{2} \tag{18}$$

(where the overdot is the derivative with respect to time), which coincides with the conventional LSW description of Ostwald ripening if $\gamma = 0$. The nonisotropic term in Eq. (17) leads to translation motion of each particle, so that

$$\dot{\mathbf{x}}_i = 2 \sum_{j=1, j\neq i}^{N} A_j \nabla G(\mathbf{x}_i - \mathbf{x}_j). \tag{19}$$

The dynamics specified by Eqs. (10), (11), (18), and (19) has a natural interpretation as a gradient flow of a reduced free energy:

$$E = \sum_{i=1}^{N} 2\pi R_i + \frac{\pi\gamma}{2}\sum_{i=1}^{N} R_i^4\left(\frac{1}{8} - \frac{1}{2}\ln R_i\right) + \frac{\gamma}{2}\sum_{i=1}^{N}\sum_{j=1, j\neq i}^{N} M_i M_j G(\mathbf{x}_j - \mathbf{x}_i), \tag{20}$$

where $M_i = \pi R_i^2$. The first term in Eq. (20) is the surface energy of each particle, whereas the second term accounts for the self-energy of the nonlocal interaction, and the third term is the particle-particle interaction energy. Note that the latter term is the same as the electrostatic energy for a system of particles with charges M_i. It can be shown (see the Appendix) that the dissipation of energy is

$$\frac{dE}{dt} = -\sum_{i=1}^{N}\sum_{j=1}^{N}\begin{bmatrix} l_{ij} & m_{ij} \\ m_{ij} & n_{ij}\end{bmatrix}\begin{bmatrix}\dot{R}_i \\ \dot{\mathbf{x}}_i\end{bmatrix}\cdot\begin{bmatrix}\dot{R}_j \\ \dot{\mathbf{x}}_j\end{bmatrix}, \tag{21}$$

where the Onsager-type coefficients are

$$l_{ii} = -2\pi R_i^2 \ln R_i, \quad m_{ii} = 0, \quad n_{ii} = M_i/2,$$
$$l_{ij} = (2\pi)^2 R_i R_j G(\mathbf{x}_i - \mathbf{x}_j), \quad m_{ij} = \pi R_j M_i \nabla G(\mathbf{x}_i - \mathbf{x}_j),$$
$$n_{ij} = 0, \quad i \neq j.$$

B. Stabilization of Ostwald ripening

The reduced system (10), (11), (18), and (19) describes both the exchange of material between particles as well as their migration. Without nonlocal effects, the system would only exhibit Ostwald ripening, whereby particles larger than average grow at the expense of smaller ones, leading to the well-known power law behavior $R \sim t^{1/3}$. On the other hand, nonlocal interactions are known to suppress this behavior [19,20,36], and particles do not continue to grow past a certain size.

The theoretical justification that Ostwald ripening will ultimately halt stems from the energy penalty of polymer stretching. To quantify this, it is instructive to ignore the interaction energy term in Eq. (20), so that the local energy contribution is, in terms of mass variables $M_i = \pi R_i^2$,

$$E_l = \sum_{i=1}^{N} 2\pi^{1/2} M_i^{1/2} + \left(\frac{\gamma}{16\pi}\right) M_i^2 [1 - 2\ln(M_i/\pi)]. \tag{22}$$

A configuration of particles which makes this energy stationary under the conservation constraint

$$\sum_{i=1}^{N} M_i = f|\Omega|$$

satisfies $\partial E_l/\partial M_i = \lambda$ where λ is a Lagrange multiplier. This implies that such a collection has uniform size distribution $M_i = M \equiv f|\Omega|/N$. This state is an energy minimizer if the Hessian of Eq. (22), which is diagonal with entries

$$\frac{\partial^2 E_l}{\partial M_i^2} = -\frac{\pi^{1/2}}{2} M_i^{-3/2} - \left(\frac{\gamma}{4\pi}\right)[1 + \ln(M_i/\pi)], \tag{23}$$

is positive definite. This occurs over an interval $M^* < M < \pi/e$, where the minimum size M^* satisfies the transcendental equation

$$M^* = \pi\left(\frac{\alpha\gamma}{2}\right)^{-2/3}, \quad \alpha = 1 + \ln(M^*/\pi). \tag{24}$$

Since α can be roughly treated as a constant, particles with radii $R > R^* \equiv (\alpha\gamma/2)^{-1/3}$ are stable to Ostwald ripening. Note that $\gamma^{-1/3}$ sets the typical length scale for particle radii over long times, so that the typical interparticle distance is $d \sim \gamma^{-1/3}(\pi/f)^{1/2}$.

The inclusion of interaction terms in the full energy (20) leads to local fluctuations in sizes which result from the heterogeneity of the nonlocal repulsive forces. It has been documented [19,20] that even after the initial coarsening phase which leads to the elimination of small particles, the approach to equilibrium leads to configurations which have a distribution of particle sizes. To illustrate this, a simulation of Eqs. (10), (11), (18), and (19) was conducted ($L = 30, \gamma = 200\,000, f = 0.1$). Consistent with early stages of microphase segregation (see also Sec. III A), we choose an initial configuration where particles have no orientational order but are uniformly distributed. This was done by subdividing the domain into small squares and randomly placing a fixed number of particles inside each square. Random placements were rejected if the interparticle spacing was either too small or too large; in particular the minimum interparticle distances

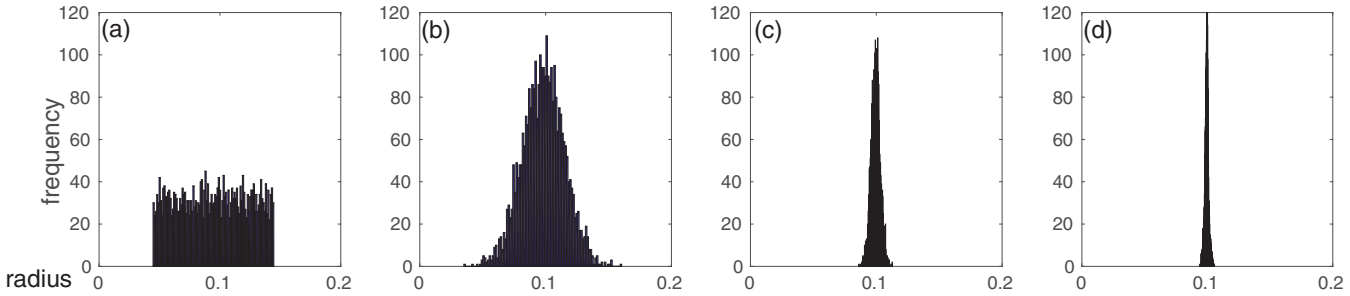

FIG. 1. (Color online) Distribution of radii (a–d) at simulation times $t = 0, 2 \times 10^{-4}, 8 \times 10^{-4}, 8 \times 10^{-3}$, respectively. Initially some particles are eliminated, but the remaining ones tend toward the average radius. This equilibration eventually halts and a small amount of size polydispersity remains.

fell into a range between 75 and 125% of the average minimum distance. Radii were chosen from a uniform random distribution on a prescribed interval.

The number of particles was initially $N = 3200$ but declined to $N = 3125$ as very small particles were eliminated. The evolution of the radii distribution is shown in Fig. 1. After the elimination phase, the distribution becomes more compact, but never becomes uniform, even after the orientational ordering process is well underway. We ascribe this to the presence of grain boundaries (see next section) composed of pattern defects that are a source of nonuniformity in the particle-particle interaction.

C. Screening effects and an efficient numerical algorithm

If our system was strictly governed by Coulomb-type repulsion, particle interactions would be long-ranged. In contrast, the exact Laplacian Green's function for a configuration of particles like Eq. (6) is known to decay exponentially in space [37]. This fact results in a screening phenomenon which may be exploited in numerical simulations.

To see how screening arises in Eqs. (10) and (11), let

$$v_i = 1/R_i + A_i \ln R_i/(2\pi), \tag{25}$$

which should be regarded as particular values $\overline{v}(x_i) = v_i$ of a smooth mean field $\overline{v}(x)$. It is useful to define the statistical distribution functions:

$$\begin{aligned} \nu(x) &= -\sum_{i=1}^{N} \frac{2\pi}{\ln R_i} \delta(x - x_i), \\ \phi(x) &= -\sum_{i=1}^{N} \frac{2\pi}{R_i \ln R_i} \delta(x - x_i). \end{aligned} \tag{26}$$

Using definition (25), the linear system (10) and (11) can be written formally as the integral equations

$$\int \phi(\mathbf{y}) - \nu(\mathbf{y})\overline{v}(\mathbf{y})\, d\mathbf{y} = -\gamma f, \tag{27}$$

$$v(\mathbf{x}) = \int G(\mathbf{x} - \mathbf{y})[-\nu(\mathbf{y})v(\mathbf{x}) - \phi(\mathbf{y})]d\mathbf{y}, \tag{28}$$

where the second is valid for each $\mathbf{x} = \mathbf{x}_i$. If the particle number density is (artificially) sent to infinity at the same time making the radii small so that ν and ϕ limit to smooth functions, the expressions (27) and (28) constitute the solution to a generalized Helmholtz equation:

$$-\Delta\overline{v} + \nu\overline{v} = \phi + \gamma f. \tag{29}$$

The corresponding Green's function of this equation decays as $\exp(-|\mathbf{x}|/l)$ where $l \approx \nu^{-1/2}$ is the screening length.

We have found that, even when the particle density is not particularly high, the system (10), (11), (18), and (19) still has a strong screening effect. To illustrate this effect, the system was initialized with the random particle array as described above. A single particle was then displaced by roughly one quarter of the interparticle distance, and the effect on coefficients A_i and velocities $d\mathbf{x}_i/dt$ of neighboring particles was measured (Fig. 2). There is a strong drop-off in the interaction strength, meaning that particles at a distance of more than about five interparticle spacings are largely unaffected by the perturbation. We have also seen a similar effect when the perturbation is applied to the particle's radius instead of its position.

As written, the linear system (10) and (11) is unsuitable for numerical solution as N grows large. By virtue of screening

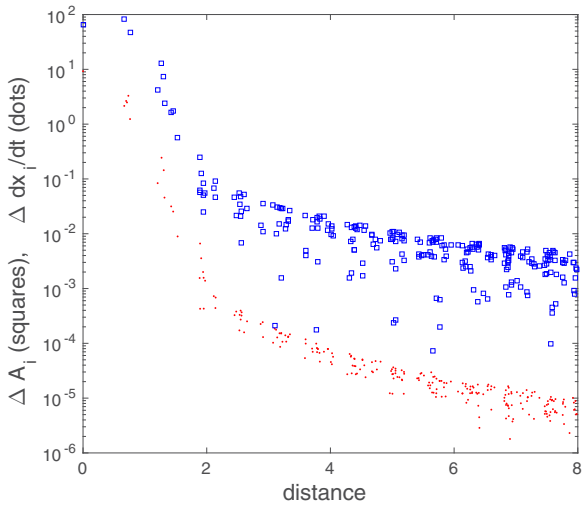

FIG. 2. (Color online) Effect on the system coefficients A_i (squares) and velocities $d\mathbf{x}_i/dt$ (dots) of particles at various distances from a perturbed particle. The effect of the perturbation drops off sharply when the distance is greater than about five interparticle spacings, and then continues to decay as a slower but exponential rate.

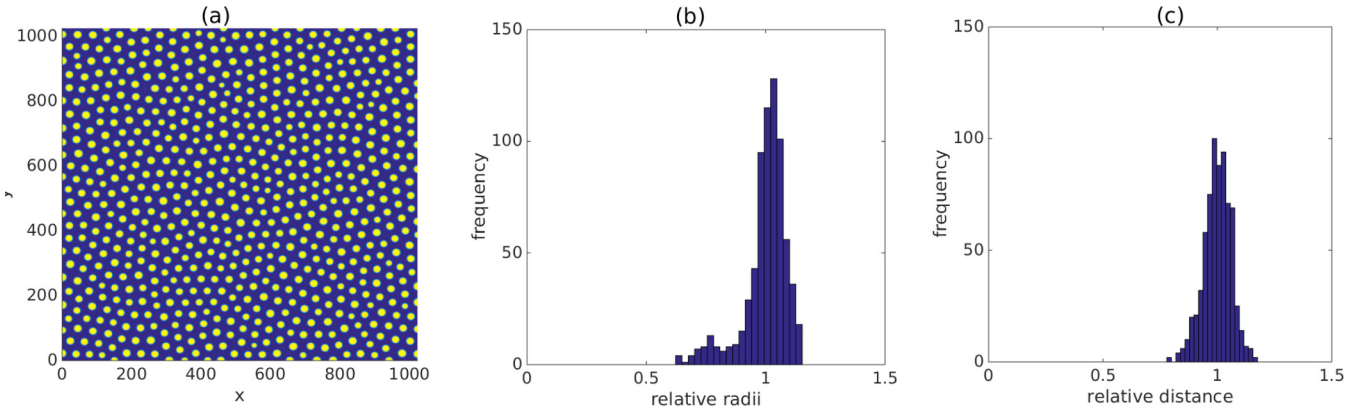

FIG. 3. (Color online) Density functional model (2) simulation up to a point where Ostwald ripening halts. (a) Density field ϕ, (b) distribution of particle radii scaled by the average radius, and (c) distribution of minimum interparticle distances scaled by their average.

effects, however, particle dynamics should only depend on the configuration of particles within a region whose size is commensurate to the screening length. In practice, this is accomplished by dividing the entire domain into subdomains, each augmented with a buffer zone of neighboring particles chosen to be somewhat larger in width than the screening length. Then smaller linear systems of the form of Eqs. (10) and (11) are solved on each subdomain. One complication is that the constraint (10) is global, and cannot be satisfied for each subdomain. Instead, we solve modified versions of Eq. (11),

$$\frac{1}{R_i} = \frac{B_i}{2\pi} \ln R_i + \sum_{j=1, j\neq i}^{N} B_j G(\mathbf{x}_i - \mathbf{x}_j),$$

$$\frac{1}{R_i} = 1 - \frac{C_i}{2\pi} \ln R_i + \sum_{j=1, j\neq i}^{N} C_j G(\mathbf{x}_i - \mathbf{x}_j),$$

on each subdomain, and then determine the coefficients as

$$A_i = (1 - A_0)B_i + A_0 C_i, \tag{30}$$

where A_0 is chosen so that Eq. (10) is satisfied. Note that this enforces global mass conservation via Eq. (18).

Rather than using Ewald summation for the periodic Green's function, we have found it easier to use an analytical approximation of the form

$$\begin{aligned} G(x,y) \approx -\frac{1}{4\pi} \ln \left[\sin\left(\frac{2\pi x}{L}\right) + \sin\left(\frac{2\pi y}{L}\right) \right] \\ + a\left[\cos\left(\frac{2\pi x}{L}\right) + \cos\left(\frac{2\pi y}{L}\right) \right] \\ + b \cos\left(\frac{2\pi x}{L}\right) \cos\left(\frac{2\pi y}{L}\right), \end{aligned}$$

where $a = -0.007$ and $b = .007$ are obtained from a least squares fit with the numerically exact Green's function. The time evolution (18) and (19) is discretized by standard finite differencing, adapting the time step so that the average particle displacement per step is roughly constant throughout the simulation. For very large time steps, there is numerical instability associated with the positional dynamics (19), and semi-implicit time stepping is used, fixing the coefficients A_i at the current time step. In the Ostwald ripening phase, we also monitor the radii and eliminate very small particles.

III. ORDERING DYNAMICS

After the initial transient stage characterized by Ostwald ripening and radii equilibration, migration of particles is the dominant effect. From this point on, the radii dynamics are "quasistatic"—they adjust quickly depending on the configuration of particles. Past this point, localized regions of hexagonal order emerge, separated by grain boundaries composed of topological defects. This section investigates and quantifies this regime.

A. Initial particle distribution

Since our interest here is in a stage of evolution where particle dynamics are dominated by migration effects, it is necessary to specify an initial configuration typical of a deeply quenched system which has already undergone Ostwald ripening. For this purpose, we use the more detailed density functional model (2), and ascertain particle statistics which are then reproduced by the choice of initial particle configurations in the reduced model.

The local density ϕ in Eq. (2) was initially chosen to represent a homogeneous mixture $\phi = f$, plus a small amount of noise. Nucleation of particles by spinodal decomposition occurs immediately, followed by a short, rapid Ostwald ripening phase. Figure 3 shows the particle configuration at the end of this process, along with distributions of radii and nearest-neighbor distances. There is no indication at this point that any orientational order has been established. On the other hand, particles are dispersed uniformly throughout the domain, with the minimum distance between particles varying only by a small amount. In addition, particle radii are also very similar.

Note that it would be impractical to use the density functional simulation to directly initialize the particle model: in Fig. 3 there are only $\approx$700 particles for a 1024^2 numerical grid. Instead, the particle simulation was initialized with a state which had identical radii, and particles chosen so that the nearest-neighbor distances were between 75 and 125% of the average distance as in the density functional simulation. We

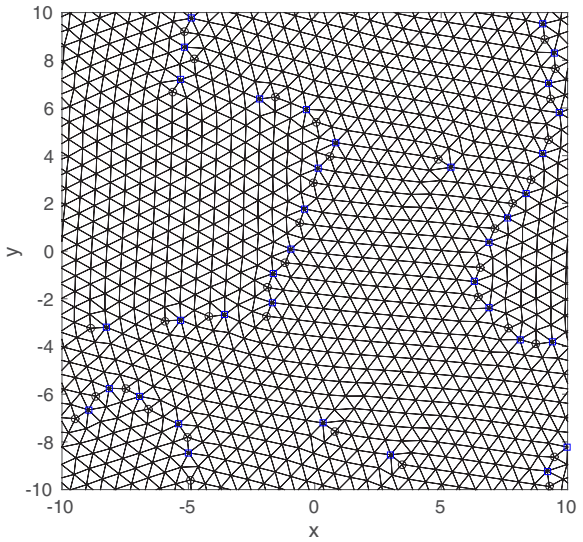

FIG. 4. (Color online) Triangulation of a small simulation ($N = 1024$, $L = 20, \gamma = 200\,000$, $f = 0.1$). Defects are identified as squares (sevenfold) and circles (fivefold).

find that the particle placement scheme outlined in Sec. II B works well for this purpose.

B. Numerical simulation

Large scale simulations ($N = 57\,344$) on a domain of size $L = 160$ were conducted (other parameters were $\gamma = 200\,000, f = 0.1$). With the choice of initial conditions given above, we find that local hexagonal ordering occurs spontaneously. As in other studies of hexagonal ordering, pattern orientation is measured using Delaunay triangulation (Fig. 4). Each edge of the triangulation has a local orientation angle θ which corresponds to a complex-valued order parameter $\Psi = \exp(6i\theta)$, which can be represented as a continuous field by interpolation. Figure 5 shows the evolution of the order parameter at four different times. There is clear evidence of the formation of domains and grain boundaries, as well as the presence of isolated defects which show up as localized inhomogeneities in the orientation field.

Triangulation also reveals the presence of topological defects. As in past studies [15,17,18], we find a prevalence of dislocations identified as pairs of fivefold and sevenfold defects (see Fig. 4). The evolution of such defects is shown in Fig. 6. Initially they are distributed evenly, but most annihilate rapidly with neighboring defects. While disclinations can theoretically be formed from isolated five- or sevenfold lattice defects, essentially none were observed here.

We have repeated the simulations under different conditions. Several runs with different random initial data yield essentially the same overall statistics. Changing the volume fraction parameter f also gave no appreciable difference in scaling. Modifying the parameter γ is equivalent to changing the domain and particle sizes, which should not have any effect on scaling of domains or defects. Finally, we note that system size should play no role here since it is much larger than any dynamic length scale.

C. Scaling of domain size and defect numbers

A typical measure of domain size can be derived from the orientation correlation function

$$g(r) = |\langle \exp[6i\theta(\mathbf{x} - \mathbf{x}')]\rangle|, \tag{31}$$

where the averages are taken over all $\mathbf{x}'$ and $|\mathbf{x} - \mathbf{x}'| = r$. We have computed this at different times in our simulation (Fig. 7). The behavior of $g(r)$ is roughly exponential:

$$g(r) \approx \exp[-r/\xi(t)]. \tag{32}$$

The orientation correlation length $\xi(t)$ was determined by least squares regression, although the fit is slightly worse for large ξ.

The time evolution of both the correlation length $\xi(t)$ and the number of five to seven defect pairs $N_d(t)$ is given in Fig. 8, along with a fit for power law dependence. At early times, the scaling exponents were roughly $1/2$ for correlation length and $-2/5$ for defect number. This corresponds to a situation where there are many free dislocations, and grain boundaries are poorly defined. The intermediate scaling regime has exponents that were between $1/5$ and $1/4$ for both correlation length and defect number. In this case, most defects exist at grain boundaries and the dynamics involves overall motion of boundaries. Finally, at large times, boundaries are pinned and the configuration becomes frozen.

D. Dislocation dynamics

The motion of dislocation defects in hexagonal systems has been studied in a variety of models [18,28,38,39]. Both dislocation glide (motion parallel to the Burger's vector) and climb have been noted in continuum models at shallow quenches [39]. In our case, only glide is observed since lattice vacancies are not energetically favored.

At the early stages of the simulation, dislocations are distributed nearly uniformly. Dislocations are removed from the system largely by pairwise annihilation. Since this can only happen if the corresponding Burger's vectors are roughly opposite in orientation, over time the system is left with subdomains which are largely free of dislocations. The boundaries of these domains have spatially correlated Burger's vectors, which appear macroscopically as grain boundaries where pattern orientation changes abruptly. At this late stage, mostly small grains are eliminated by a collective motion of defect structures.

Other theoretical studies [18,28] have noted that the motion of individual dislocations can be inhibited by spatial oscillations of driving forces. These arise from the underlying lattice structure, and are analogous to the Peierls-Nabarro forces of atomic crystals. We find that in general dislocation pinning becomes relevant at later times, when the typical length scale for interaction between grain boundaries is large. Eventually this causes the entire lattice to become frozen.

Dislocations interact through strains which they generate. This interaction is in general a collective effect of many defects, and is presumably mediated by some kind of cancelation or screening effect. We postulate the existence of an interaction length scale $\xi_d(t)$, different than the correlation length $\xi(t)$, which characterizes the typical distance over which dislocations interact. At early stages, there is little correlation

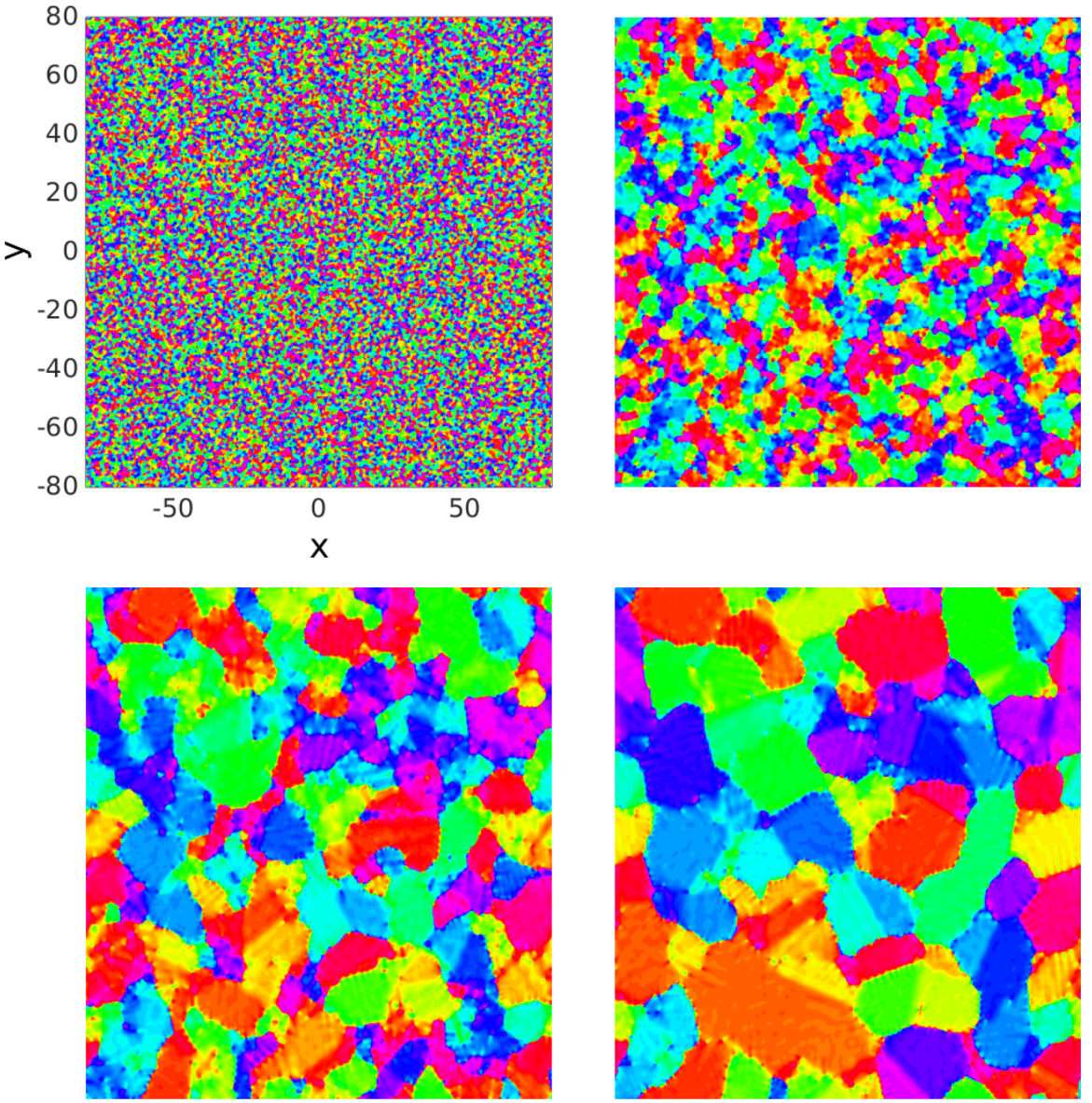

FIG. 5. (Color online) Evolution of the pattern orientation order parameter $\Psi = \exp(6i\theta)$ at times $t = 4.0 \times 10^{-4}, 6.2 \times 10^{-2}, 0.95, 10.1$. The coloration represents a HSV map of angles $0 \leqslant \theta < \pi/3$ ($N = 57\,344$, $L = 160$, $\gamma = 200\,000$, $f = 0.1$).

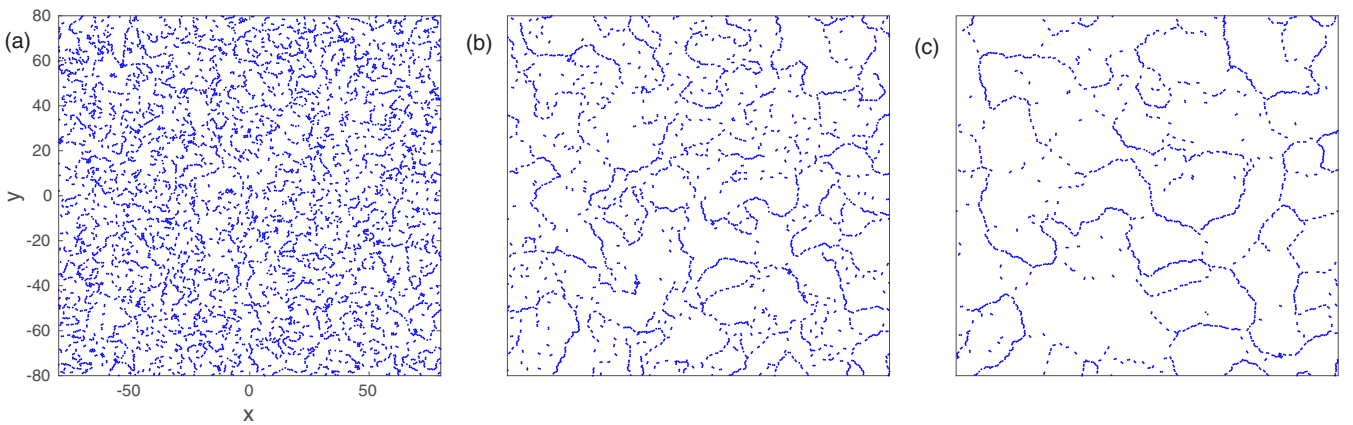

FIG. 6. (Color online) (a–c) Evolution of dislocation defects at times $t = 6.2 \times 10^{-2}, 0.95, 10.1$, respectively. Simulation parameters are the same as in the previous figure.

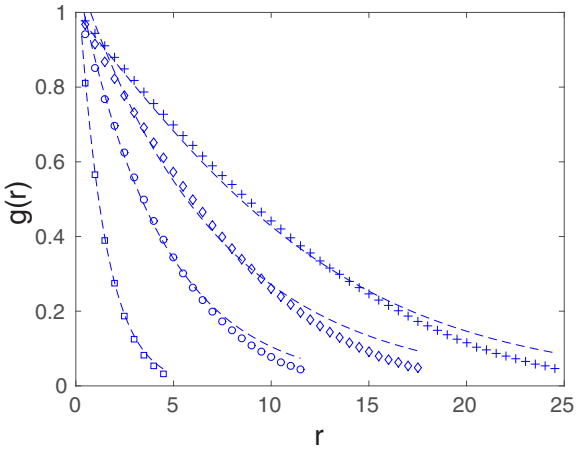

FIG. 7. (Color online) The orientation correlation function $g(r)$ at times $t = 0.05,0.5,5,50$ (squares, circles, diamonds, $+$). The dashed line shows the least squares fit to an exponential $g(r) \approx \exp[(r/\xi(t)]$.

between nearby dislocation orientations (as measured by their Burger's vectors). This should imply that ξ_d is proportional to the distance between defects. Note that at early stages local orientational ordering can take place despite the proximity of defects, and so a more rapid scaling of ξ is expected. On the other hand, when grain boundaries are well developed, neighboring dislocations which comprise the same grain boundary do not generally contribute to each other's dynamics. In this case, both length scales ξ and ξ_d should be on the order of the grain size instead.

E. Crossover of dynamic scaling

We now propose a model for the scaling of defect evolution which is consistent with both the early and intermediate ordering stages. It is reasonable to suppose that the dynamics scale (in a statistically averaged fashion) as a function of defect correlation length:

$$\frac{dx}{dt} \propto \xi_d^{-\beta},$$

where the exponent β is to be determined empirically. This relationship cannot be simply derived from the forces created by dislocations, since dynamics are both a function of energetic driving forces as well as dissipation from large-scale lattice motion (e.g., [22]).

In the early stage of ordering, defects are distributed nearly homogeneously, which means that $\xi_d \propto N_d^{-1/2}$. If defects move at a rate proportional to $\xi_d^{-\beta}$, then the characteristic time it takes for defects to collide and annihilate will be proportional to $\xi_d^{1+\beta}$. The resulting rate of defect annihilation scales as $\xi_d^{-\beta-1} \propto N_d^{(\beta+1)/2}$. Under the assumption that annihilation events are uncorrelated, it follows that

$$\frac{1}{N_d}\frac{dN_d}{dt} \propto N_d^{(\beta+1)/2}, \tag{33}$$

which means (upon integration) that the defect number scales as $N_d \propto t^{-2/(1+\beta)}$. To be empirically consistent with the observed scaling exponent $N_d \propto t^{-2/5}$, one would need $\beta = 4$.

In the intermediate stage of phase ordering, defects are primarily distributed along grain boundaries. If the line density of dislocations is taken constant along the grain boundary, this means that $\xi_d \propto N_d^{-1}$, in contrast to the early stage. This arises from the fact that the number of domains N_g scales as ξ_d^{-2} and $N_g \xi_d \propto N_d$. In this case, the rate of defect annihilation satisfies

$$\frac{1}{N_d}\frac{dN_d}{dt} \propto N_d^{\beta+1}, \tag{34}$$

which leads to $N_d \propto t^{-1/(\beta+1)}$. If dynamics are consistent with the early-stage exponent $\beta = 4$, then the scaling exponent for N_d would be $-1/5$. This is close to, but smaller than,

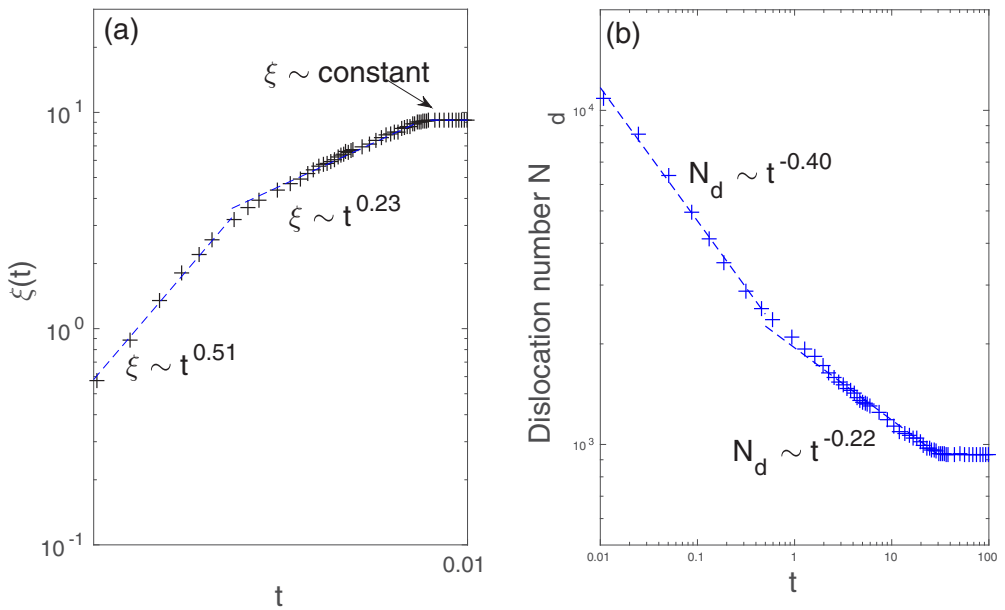

FIG. 8. (Color online) (a) Evolution of the orientation correlation length. (b) Evolution of defect number. Power law regression is shown as dashed lines. In both cases, three different scaling regimes can be seen.

the empirically observed scaling exponent of ≈ -0.22. On the other hand, some of the assumptions made prior are not exactly correct. One factor which may enhance the rate of phase ordering is that a small fraction of dislocations are in fact not on grain boundaries. This mean that the true picture should interpolate between scaling exponents described by Eqs. (33) and (34).

F. Comparison to experiment and other models

Harrison *et al.* [15] observed ordering in spherical block copolymer microdomains in a thin film by atomic force microscopy. They find over the bulk of the observed time frame that the orientational correlation length ξ exhibits a roughly $t^{1/4}$ growth law, whereas dislocation density decreases as roughly $t^{-1/5}$. Ji *et al.* [16] performed similar observations on cylinder forming copolymer thin films. They find growth exponents slightly larger than $t^{1/4}$ under a variety of conditions.

Simulation of a reduced system similar to ours, but corresponding to a different interaction term, was done by Sagui and Desai [40]. There the measured growth exponent for orientational correlation length was much closer to $1/2$. We believe this represents a difference in the underlying model as well as simulation sizes much smaller than ours.

The cell dynamics model of Yokojima and Shiwa [17] yields a scaling exponent for orientational correlation length closer to $1/5$. Notably, this model incorporates hydrodynamic effects, rather than the purely diffusive kinetics considered here and elsewhere. Hydrodynamics are known to accelerate phase formation and ordering of three dimensional block copolymer microstructures [41] as well as films with lamellar morphology [17,42]. On the other hand, in [17] it is concluded that their role is subdominant for hexagonal films and insufficient to alter the growth law.

In contrast, the diffusion-driven cell dynamics model in Vega *et al.* [18] includes noise to mimic thermal fluctuations and gives a scaling exponent closer to $1/4$. Since fluctuations are relatively less important in the strong segregation limit and are not included here, it is not surprising that our results have a smaller exponent.

Both the experiments in [15] and simulations in [17] also show a distinct rapid stage of ordering at early times, which the authors do not quantify. Li *et al.* [43] also performed cell dynamics simulations with and without a prescribed driving potential. Without the driving force, they see a two stage process characterized by rapid $t^{-1/3}$ defect coarsening initially followed by slower $t^{-1/5}$ coarsening at late stages.

Although experiments show some indication of slowing at the late stages of the observed time period, none observe a perfectly frozen configuration. Gómez *et al.* [44] find a regime in a density functional model where correlation lengths grow logarithmically. They ascribe this behavior to a Lifshitz-Safran picture of triple-junction dynamics rather than dislocation pinning, however.

IV. CONCLUSION

We have shown that phase ordering in the strongly segregated spherical phase of block copolymers exhibits three different stages of dynamic behavior. Initially unaligned topological defects tend to annihilate. This mostly leaves aligned dislocations which constitute grain boundaries. We propose that this configurational change results in a crossover in scaling because the dependence of dislocation density on interaction distance changes.

Theoretical explanations for slow coarsening exponents in grain boundary evolution are a well known puzzle in a variety of systems, including atomistic and experimental systems [45,46]. While our interacting particle system is much different than the continuum models used in most prior theoretical studies of two dimensional hexagonal ordering, it appears to exhibit slow coarsening behavior with similar exponents. We speculate that this is a combined effect of energy dissipation associated with bulk lattice rearrangement as well as pinning forces.

It is challenging but worthwhile to look for a more rigorous link between the dynamic Ohta-Kawasaki model (2) and the reduced dimensional particle model. Some results in this direction exist for the pure LSW system which exhibits only Ostwald ripening [47]. On the other hand, the particle model could be viewed as a reasonable description in its own right since it (1) correctly describes mass transfer between particles and (2) dissipates energy in the correct way for diffusive kinetics.

Finally it is worth mentioning physical mechanisms which enhance the rate of ordering of block copolymer films. One avenue of research is self-assembly, which seeks to direct microstructure evolution using topographically or chemically patterned templates [48]. Copolymer nanostructures may also be controlled by external electric fields [49], which includes the ability to direct pattern orientation. Ordering dynamics in these controlled situations could likely be studied in the context of the present methodology.

ACKNOWLEDGMENT

This work was performed under NSF award DMS-1514689.

APPENDIX: COMPUTATION OF ENERGY DISSIPATION

The time derivative of Eq. (20) is

$$\begin{aligned}\frac{dE}{dt} &= \sum_{i=1}^{N}(2\pi - \gamma\pi R_i^3 \ln R_i)(\dot{R}_i) \\ &\quad + \frac{\gamma}{2}\sum_{i=1}^{N}\sum_{j=1,j\neq i}^{N}(2\pi R_i)\dot{R}_i M_j G(\mathbf{x}_j - \mathbf{x}_i) \\ &\quad + \gamma\sum_{i=1}^{N}\sum_{j=1,j\neq i}^{N} M_i M_j \nabla G(\mathbf{x}_i - \mathbf{x}_j)\cdot\dot{\mathbf{x}}_i. \qquad \text{(A1)}\end{aligned}$$

It is convenient to introduce the quantities $\mu_i = A_i + \gamma\pi R_i^2 = A_i + \gamma M_i$, which represent the expansion coefficients of the chemical potential $\mu = \sum_i \mu_i G(\mathbf{x} - \mathbf{x}_i)$. Then using Eq. (18) we can write $\mu_i = -2\pi R_i \dot{R}_i$, which means that the linear system (11) is the same as

$$\begin{aligned}2\pi - \gamma\pi R_i^3 \ln R_i &= 2\pi A_0 R_i - \mu_i R_i \ln R_i \\ &\quad + 2\pi R_i \sum_{j=1,j\neq i}^{N}\left(\mu_j - \gamma\pi R_j^2\right)G(\mathbf{x}_i - \mathbf{x}_j). \qquad \text{(A2)}\end{aligned}$$

With $\gamma M_j = A_j - \mu_j$, the last term in Eq. (A1) becomes [using Eq. (19)]

$$\gamma \sum_{i=1}^{N} \sum_{j=1, j\neq i}^{N} M_i M_j \nabla G(\mathbf{x}_i - \mathbf{x}_j) \cdot \dot{\mathbf{x}}_i = \sum_{i=1}^{N} M_i \dot{\mathbf{x}}_i \cdot \left[\sum_{j=1, j\neq i}^{N} \mu_i \nabla G(\mathbf{x}_i - \mathbf{x}_j) \right] - \sum_{i=1}^{N} \frac{M_i}{2} |\dot{\mathbf{x}}_i|^2. \tag{A3}$$

Using Eqs. (A2) and (A3), the expression (A1) can be written as Eq. (21). Provided R_i are all small enough, the matrix in Eq. (21) can be shown to be diagonally dominant and positive definite, which ensures that $dE/dt \leqslant 0$.

[1] M. P. Stoykovich, M. Müller, S. O. Kim, H. H. Solak, E. W. Edwards, J. J. De Pablo, and P. F. Nealey, Science **308**, 1442 (2005).
[2] T. Smart, H. Lomas, M. Massignani, M. V. Flores-Merino, L. R. Perez, and G. Battaglia, Nano Today **3**, 38 (2008).
[3] H.-C. Kim, S.-M. Park, and W. D. Hinsberg, Chem. Rev. **110**, 146 (2009).
[4] J. K. Kim, S. Y. Yang, Y. Lee, and Y. Kim, Prog. Polym. Sci. **35**, 1325 (2010).
[5] A. Blanazs, S. P. Armes, and A. J. Ryan, Macromolecular Rapid Communications **30**, 267 (2009).
[6] Y. Mai and A. Eisenberg, Chem. Soc. Rev. **41**, 5969 (2012).
[7] F. Bates and G. H. Fredrickson, Phys. Today **52**, 32 (1999).
[8] M. W. Matsen and F. S. Bates, Macromolecules **29**, 1091 (1996).
[9] G. H. Fredrickson, *The Equilibrium Theory of Inhomogeneous Polymers* (Clarendon, Oxford, 2006).
[10] I. W. Hamley, *The Physics of Block Copolymers* (Clarendon, Oxford, 1998).
[11] M. W. Matsen and M. Schick, Phys. Rev. Lett. **72**, 2660 (1994).
[12] R. Choksi, M. A. Peletier, and J. Williams, SIAM J. Appl. Math. **69**, 1712 (2009).
[13] R. A. Segalman, Mater. Sci. Eng. R **48**, 191 (2005).
[14] C. Harrison, Z. Cheng, S. Sethuraman, D. A. Huse, P. M. Chaikin, D. A. Vega, J. M. Sebastian, R. A. Register, and D. H. Adamson, Phys. Rev. E **66**, 011706 (2002).
[15] C. Harrison, D. Angelescu, M. Trawick, Z. Cheng, D. Huse, P. Chaikin, D. Vega, J. Sebastian, R. Register, and D. Adamson, Europhys. Lett. **67**, 800 (2004).
[16] S. Ji, C.-C. Liu, W. Liao, A. L. Fenske, G. S. Craig, and P. F. Nealey, Macromolecules **44**, 4291 (2011).
[17] Y. Yokojima and Y. Shiwa, Phys. Rev. E **65**, 056308 (2002).
[18] D. A. Vega, C. K. Harrison, D. E. Angelescu, M. L. Trawick, D. A. Huse, P. M. Chaikin, and R. A. Register, Phys. Rev. E **71**, 061803 (2005).
[19] C. Sagui and R. C. Desai, Phys. Rev. E **52**, 2822 (1995).
[20] K. Glasner and R. Choksi, Physica D **238**, 1241 (2009).
[21] R. Backofen, K. Barmak, K. E. Elder, and A. Voigt, Acta Materialia **64**, 72 (2014).
[22] A. Adland, Y. Xu, and A. Karma, Phys. Rev. Lett. **110**, 265504 (2013).
[23] K. R. Elder and M. Grant, Phys. Rev. E **70**, 051605 (2004).
[24] K. R. Elder, J. Viñals, and M. Grant, Phys. Rev. Lett. **68**, 3024 (1992).
[25] M. C. Cross and D. I. Meiron, Phys. Rev. Lett. **75**, 2152 (1995).
[26] Q. Hou, S. Sasa, and N. Goldenfeld, Physica A (Amsterdam) **239**, 219 (1997).
[27] D. Boyer and J. Vinals, Phys. Rev. E **64**, 050101 (2001).
[28] D. Boyer and J. Vinals, Phys. Rev. Lett. **89**, 055501 (2002).
[29] T. Ohta and K. Kawasaki, Macromolecules **19**, 2621 (1986).
[30] L. Leibler, Macromolecules **13**, 1602 (1980).
[31] T. Uneyama and M. Doi, Macromolecules **38**, 5817 (2005).
[32] Y. Nishiura and I. Ohnishi, Physica D **84**, 31 (1995).
[33] C. B. Muratov, Phys. Rev. E **66**, 066108 (2002).
[34] I. M. Lifshitz and V. V. Slyozov, J. Chem. Phys. Solids **19**, 35 (1961).
[35] C. Wagner, Z. Elektrochemie **65**, 581 (1961).
[36] L. Q. Chen and A. G. Khachaturyan, Phys. Rev. Lett. **70**, 1477 (1993).
[37] B. Niethammer and J. J. L. Velázquez, Arch. Ration. Mech. Anal. **180**, 493 (2006).
[38] L. S. Tsimring, Physica D **89**, 368 (1996).
[39] A. D. Pezzutti, D. A. Vega, and M. A. Villar, Phil. Trans. R. Soc. A **369**, 335 (2011).
[40] C. Sagui and R. C. Desai, Phys. Rev. E **52**, 2807 (1995).
[41] T. Honda and T. Kawakatsu, J. Chem. Phys. **129**, 114904 (2008).
[42] I. Podariu, Z. Shou, and A. Chakrabarti, Phys. Rev. E **62**, R3059 (2000).
[43] W. Li, F. Qiu, Y. Yang, and A.-C. Shi, Macromolecules **43**, 1644 (2010).
[44] L. R. Gómez, E. M. Vallés, and D. A. Vega, Phys. Rev. Lett. **97**, 188302 (2006).
[45] K. Barmak, E. Eggeling, D. Kinderlehrer, R. Sharp, S. TaAsan, A. Rollett, and K. Coffey, Prog. Mater. Sci. **58**, 987 (2013).
[46] E. A. Holm and S. M. Foiles, Science **328**, 1138 (2010).
[47] B. Niethammer, F. Otto, and J. J. Velázquez, in *Analysis, Modeling and Simulation of Multiscale Problems* (Springer, New York, 2006), pp. 501–530.
[48] J. Y. Cheng, C. A. Ross, H. I. Smith, and E. L. Thomas, Adv. Mater. **18**, 2505 (2006).
[49] C. Liedel, C. W. Pester, M. Ruppel, V. S. Urban, and A. Böker, Macromol. Chem. Phys. **213**, 259 (2012).